remote sensing

Article

Effusion Rates on Mt. Etna and Their Influence on Lava Flow Hazard Assessment

Francesco Zuccarello *, Giuseppe Bilotta, Annalisa Cappello and Gaetana Ganci

Istituto Nazionale di Geofisica e Vulcanologia, Osservatorio Etneo, 95125 Catania, Italy; giuseppe.bilotta@ingv.it (G.B.); annalisa.cappello@ingv.it (A.C.); gaetana.ganci@ingv.it (G.G.)
* Correspondence: francesco.zuccarello@ingv.it

Abstract: The rate at which lava is discharged plays a key role in controlling the distance covered by lava flows from eruptive vents. We investigate the available time-averaged discharge rates (TADRs) estimated for recent flank eruptions at Mt. Etna volcano (Italy), in order to define a possible generalized effusion rate trend which is consistent with observed real data. Our analysis indicates a rapid waxing phase in which effusion rate peaks occur for between 0.5 and 29% of the total eruption time, followed by a progressive decrease in the waning phase. Three generalized curves are built by calculating the 25th, 50th and 75th percentiles values associated with the occurrence of effusion peaks, and with the slope variations of descending curves in the waning phase. The obtained curves are used as an input for the GPUFLOW model in order to perform numerical simulations of the lava flows paths on inclined planes, and are compared with those generated by using effusion rate curves with a bell-shaped time-distribution. Our tests show how these characteristic curves could impact single-vent scenarios, as well as short- and long-term hazard maps, with maximum variations of up to 40% for a specific category of eruptive events.

Keywords: lava flows; flank eruptions; trend analysis; numerical simulations

Citation: Zuccarello, F.; Bilotta, G.; Cappello, A.; Ganci, G. Effusion Rates on Mt. Etna and Their Influence on Lava Flow Hazard Assessment. *Remote Sens.* **2022**, *14*, 1366. https://doi.org/10.3390/rs14061366

Academic Editor: David Gomez-Ortiz

Received: 3 February 2022
Accepted: 8 March 2022
Published: 11 March 2022

1. Introduction

Lava flows are recurring and widespread hazards affecting areas around active volcanoes, which can cause significant social and economic loss. In the last decades, advances in the knowledge of the physical parameters controlling the evolution of flowing lava allowed the development of physics-based models of lava flows, which have been proven to be effective to forecast and assess the hazard posed by effusive events (e.g., [1–4]). Such numerical simulations can be adopted for real-time applications by forecasting in a few minutes the expected path that flowing lava could cover in days or weeks during an on-going eruption [5–8]. Alternatively, they constitute a powerful tool for the evaluation of the long-term hazard through the development of lava flows hazard maps (e.g., [9,10]). These models require different input parameters, such as the physical properties of the fluid (e.g., melt compositions, water content, rheological law, thermal properties) and the topography of the terrain. A critical parameter in physical-mathematical modelling is the effusion rate, i.e., the rate at which the lava is discharged. The lava effusion rate is variable in time, strongly controlling the emplacement and run-out distance of lava flows. Generally, greater lengths of lava flows are correlated with high lava effusion rates [11,12], and at basaltic volcanoes lava discharge occurs at high rates during the early phases of eruptions, followed by a slow decrease towards the end [13,14]. Nevertheless, both for the assessment of long-term hazards and for monitoring efforts during on-going eruptions, the effusion rate is assumed to be constant or to have a bell-shaped time-dependent behavior [10,15].

Various approaches have been adopted to estimate lava effusion rates, including volume-based measurements and thermal approaches [16]. The first is based on the reconstruction of the morphological evolution of the lava field, in which time-averaged discharge rates (TADRs, i.e., the effusion rate averaged over given periods) are estimated by calculating the partial volume of lava which erupted in defined time spans (e.g., [17–19]). Partial lava volumes are obtained by determining the thickness and covered area of the different portions of lava flows through field measurements or, if available, by comparing pre- and post-eruption topographic surfaces. The accuracy of lava volume estimation, depending on the quality and density of field measurements, as well as on the spatial resolution of topographic models, and the poor temporal resolution of TADR measurements constitute the major sources of uncertainties. More recently, TADR temporal series have been derived from satellite thermal infrared data [20–24]. The detection of hotspot pixels allows the recognition of the volcanic area affected by thermal anomalies associated with the flowing lava, and the total radiant heat flux is converted into TADRs [20]. The advantage of using this approach is a near real-time estimation of the lava effusion rate, proving to be useful as a monitoring tool of volcanic activity [25,26]. The main limitation of this approach is the dependency on atmospheric conditions, such as the presence of clouds impacting the detection of hotspot pixels and the associated heat flux.

Mt. Etna (Italy) is one of the most active and best-monitored basaltic volcanoes worldwide, and is characterized by both persistent degassing and explosive activity at the summit alternating with recurrent flank eruptions (e.g., [27,28]). The latter represent the major source of hazard for the densely populated areas around the volcano due to the emission of basaltic lava at vents located at the lower heights, with higher probabilities to impact the inhabited areas. Here, we present an analysis of the TADRs for the best-documented flank eruptions in the last century at Mt. Etna (11 eruptions), using data from both field measurements and satellite thermal imagery, in order to define a possible generalized effusion rate trend to be used for the physical modeling of lava flows. This analysis provides insights into the eruptive dynamics of the volcano and tools to improve the assessment of lava flow hazards both in nowcasting scenarios and for long-term maps.

2. Materials and Methods

The generalization of the effusion rate curve for flank eruptions at Mt. Etna was performed by analyzing the 1928, 1981, 1983, 1985, 1986–87, 1991–93, 2001, 2002–03 (south flank), 2004–05, 2008–09 and 2018 effusive events. The effusion rates provided for the 1928 [19] and the 1981 eruptions [17] were obtained by the reconstruction of the evolution of the lava flows emplacement. The TADRs for the 1983, 1985, 1986–87, 1991–93 and 2002–03 (south flank) eruptions were estimated by converting the thermal data collected by the AVHRR sensor, which is characterized by a minimum temporal resolution of 12 h [14]. For the other post-2000 eruptions, the TADRs data were estimated through the HOTSAT system [22,29], which uses infrared radiation collected by MODIS (2001 eruption [30]) and SEVIRI sensors (2004–05, 2008–09 and 2018 eruptions [31–33]). The main parameters for the best-documented Etnean flank eruptions that occurred in the last century and used in this study are summarized in Table 1.

In order to obtain homogeneous curves in the duration and sampling times, reducing redundancies and improving data consistency, we normalized both the time data (dividing by the total duration) and the TADR amplitude (dividing by the maximum value) for each eruption. However, due to the different temporal resolutions of the satellite sensors, the satellite-derived TADRs are characterized by oscillations at different frequencies, making it challenging to define a general trend for all of the investigated eruptions (Figure 1). Even though such oscillations can be due to actual variations in effusion rates, other factors, such as atmospheric effects or the presence of volcanic clouds, could result in a high variability of the TADR curves [22]. Because we are interested in defining an overall trend for all of the selected eruptive episodes, each time series derived from the satellite has been convoluted by selecting local positive peaks, avoiding negative peaks related to the potentially underestimated TADRs (Figure 2a). Additionally, for the 2004–05, 2008–09 and 2018 eruptions, data provided by SEVIRI sensors were collected every ~15 min, producing huge time series characterized by several oscillations at various frequencies.

In these cases, high-frequency noise was removed by performing a filtering in the frequency domain (Figure 2b) using the PeakFit package software by Jandel Scientific [34] before the convolution and normalization.

Table 1. Start and end date, duration, volume, effusion rate peak and reference for the investigated flank eruptions at Mt. Etna.

Eruption	Start Date	End Date	Duration (Days)	Volume ($\times 10^6$ m^3)	Effusion Rate Peak (m^{3}s^{-1})	Reference
1928 (Lower fissure)	4 November 1928	19 November 1928	15	53	374.4	[19]
1981	17 March 1981	23 March 1981	6	23	641.4	[17]
1983	27 April 1983	16 October 1983	131	62	50.0	[14]
1985	12 March 1985	13 July 1985	124	15	3.2	[14]
1986–87	30 October 1986	27 February 1987	120	82	13.0	[14]
1991–93	14 December 1991	30 March 1993	471	183	13.5	[14]
2001 (Calcarazzi system)	17 July 2001	9 August 2001	23	38	34.3	[30]
2002–03 (south flank)	27 October 2002	29 January 2003	94	50	39.2	[14]
2004–05	7 September 2004	8 March 2005	182	64	21.5	[31]
2008–09	13 May 2008	7 July 2009	420	68	15.6	[32]
2018	24 December 2018	27 December 2018	4	2.5	80.2	[33]

Normalized averaged curves were built by taking the 25th, 50th and 75th percentiles associated with the occurrence of the effusion rate peaks, time and slope change of the analyzed curves with respect to the total time, as described in the Results section below. Then, these normalized curves were converted into real-time effusion rates to be used as an input for the GPUFLOW model [35], an improved version of the MAGFLOW cellular automaton [4,36] that features several enhancements such as support for landslides and pyroclastic density currents, and an improved thermo-rheological model for lava flows including a variable emissivity model and a windchill parameter. In addition to the effusion rate, the input parameters required by GPUFLOW are the physical properties of lava (density, eruption and solidus temperatures, water content), the digital topography over which the lava is emplaced, and the locations of eruptive vent(s) or fissure(s).

In order to quantify the difference in the emplacement and run-out distance of the simulated lava flows exclusively as a function of the effusion rate coupled with the effects of the slope on which the lava is flowing, we performed a sensitivity analysis by running all of the simulations on three flat planes with different inclinations (10°, 20° and 30°), which are consistent with the mean slopes of the volcanic edifice. The other input parameters, in particular the physical properties of the lava, were kept constant for all of the simulations, using averaged values within the possible ranges of the variations defined for Etnean lavas (density: 2600 kg·m^{-3}; solidus temperature: 1143 K; eruption temperature: 1360 K; water concentration: 0.1 wt.% [4]). The spatial resolution of inclined planes is 10 m.

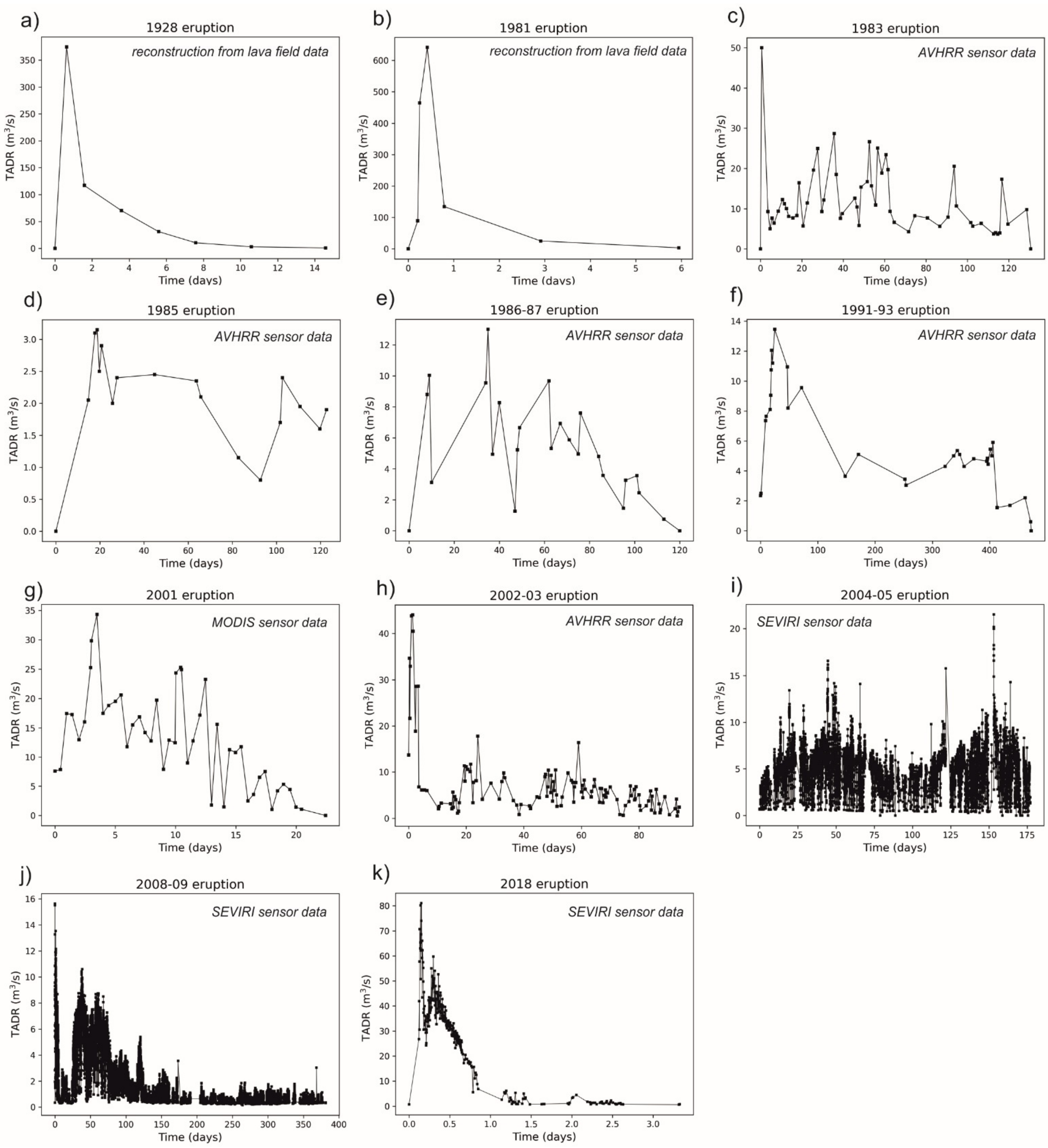

Figure 1. Estimated TADR time series related to the flank eruptions at Mt. Etna from field measurements (**a**,**b**), from AVHRR sensor (**c**–**f**,**h**), from MODIS sensor (**g**) and from SEVIRI sensor (**i**–**k**). See Table 1 for references.

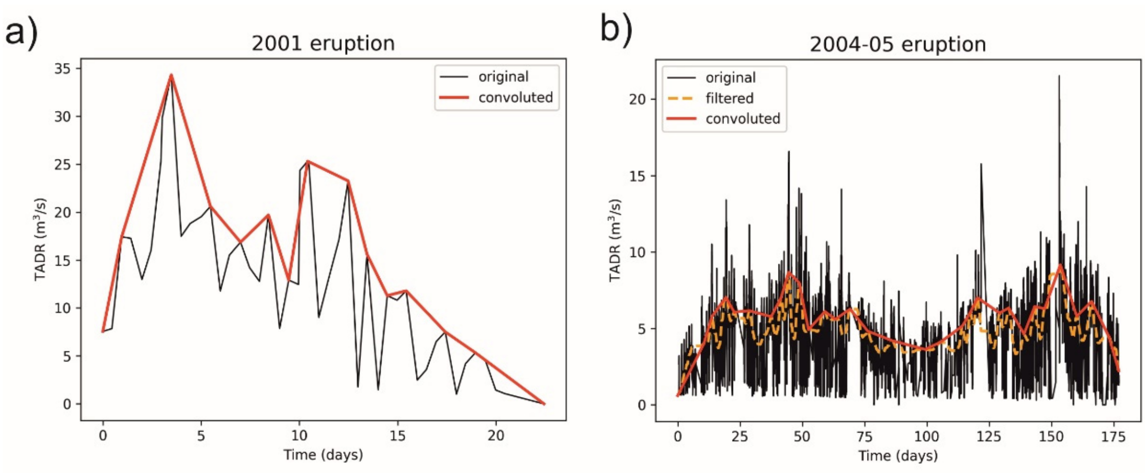

Figure 2. Examples of (**a**) convoluted and (**b**) filtered (dashed orange line) and convoluted (red line) TADR curves estimated from the satellite infrared data.

3. Results

3.1. Analysis of the TADR Curves

Normalized TADR curves are easier to compare in terms of time variations in effusion rates among the investigated eruptions. The total duration ranges vary from 4 (2018 eruption) to 471 days (1991–93 eruption), while the peaks of the effusion rates vary from 3.2 m^3s^{-1} (1985 eruption) to 641.4 m^3s^{-1}, (1981 eruption). Thus, the normalization allows the determination of when the peak of the effusion rate and the eventual slope curve changes occur relative to the total duration of the eruption.

The calculation of the percentage cumulative frequency indicates that most effusion rate peaks are observed during the initial phases of eruptions: 45% of the peaks occur in the first 5% of the total eruption duration, 64% of the peaks in the first 10%, 82% occur in the first 20%, and 91% occur in the first 30%. The calculation of 25th, 50th, 75th, 90th and 95th percentiles of the incidence of the peaks highlights a strong asymmetry in the distribution of the peaks, occurring respectively in the first 2.8%, 5.2%, 16.2%, 29.2% and 57.9% of the total duration (Figure 3).

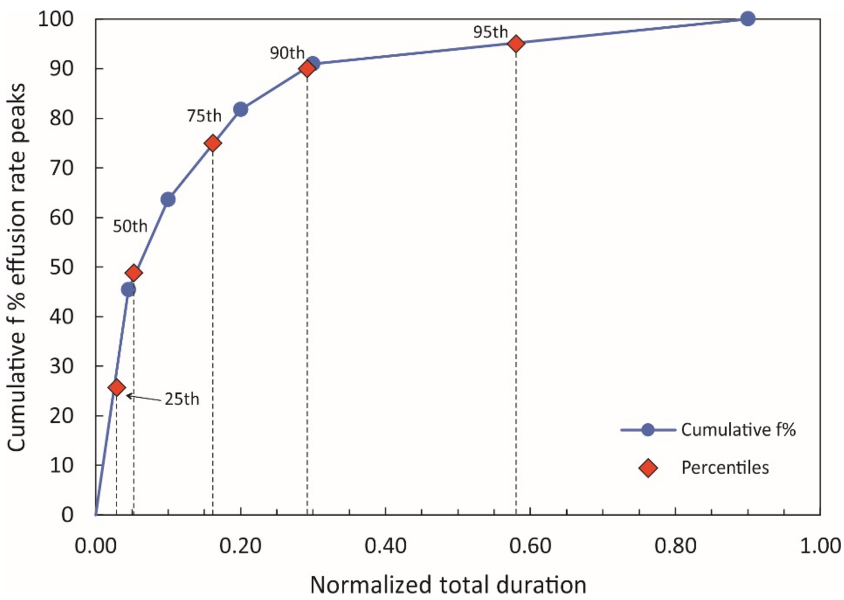

Figure 3. Plot of the percentage cumulative frequency of the effusion rate peaks' occurrence, and the corresponding 25th, 50th, 75th, 90th and 95th percentiles.

By analyzing the shape of the investigated curves, at least two trends can be recognized. Trend 1 (Figure 4a) includes the 1928, 1981, 1983, 1991–93, 2002–03 (south flank), 2008–09 and 2018 eruptions: a rapid initial waxing phase with peaks localized between 0.5% and 5% of the total eruption time is followed by a longer waning phase with a nearly exponential trend, characterized by relatively low effusion rates (average/peak ratio ~0.10–0.41), although some oscillations at low frequencies still affect some curves (e.g., 1983, 2008–09 eruptions). Trend 2 (Figure 4b) includes the 1985, 1986–87 and 2001 eruptions, which show a longer waxing phase with the peaks localized between 15% and 29% of the total duration, followed by a slower decrease in the effusion rate (average/peak ratio ~0.36–0.55). Only the effusive 2004–05 eruption showed a different behavior, characterized by a large oscillation with the occurrence of the peak at 87% of the total eruption duration.

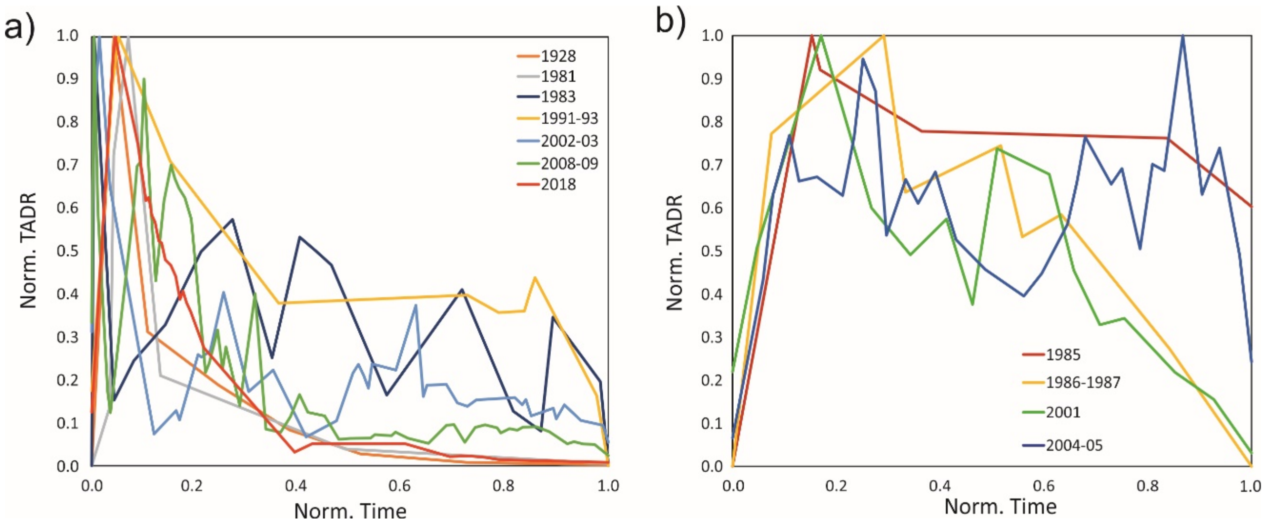

Figure 4. Diagrams showing the filtered, convoluted and normalized TADRs, where two trends can be recognized: (**a**) Trend 1, characterized by effusion rate peaks between the first 0.5% and 5% of the total eruption duration, followed by a decrease in the TADRs with an exponential trend; (**b**) Trend 2, where the effusion rate peak is observed between 15% and 29% of the total eruption duration, followed by a more progressive decrease of the TADR.

The variations of the slope for all of the effusion rate curves were evaluated by approximating the first derivatives through divided differences between consecutive pairs of sampled points. The minimum value calculated through this numerical differentiation of each curve corresponds to the inflection point of the waning phase. Most curves are characterized by initial elevated positive values of the numerical derivative, followed by a sudden decrease to negative values within 50% of the total duration, and finally by a progressive increase. Some curves (i.e., the 1983, 2004–05, 2008–09 eruptions, and to a lesser extent the 2001 and 2002–03 eruptions) show a more oscillating trend, making it more difficult to identify the inflection points (Figure 5).

3.2. Definition of "Characteristic" Effusion Rate Curves

We defined the characteristic effusion rate curves by assuming a behavior that initially increases up to a peak, decreasing with one slope until the inflection point, and then further decreasing to 0. Due to the small number of time series available for the two identified trends, a single curve for both trends was defined by taking the peak and inflection points at the 50th percentile of peaks and inflection points, considering all of the curves (regardless of trend) where the inflection point can be easily identified, thus excluding the 1983, 2004–05 and 2008–09 eruptions. The resulting normalized curve is characterized by a peak occurring at 5.2% and an inflection point occurring at 24.7% of the total eruption duration, with the inflection point reaching a value that is 49% of the peak. Two further curves were built by calculating, respectively, the 25th and 75th percentiles of occurrence of the peaks and inflection points, in order to take into account the variability of the investigated TADRs series for the sensitivity analyses. We found that the resulting 25th curve is more similar to Trend 1 (in particular, to the 1928, 1981 and 2018 eruptions), with a sharper peak at 2.8% and an inflection point at 17.6% of the total eruption duration. The effusion rate at the inflection point is only 27.1% of the peak, and then decreases progressively to zero toward the end. On the contrary, the resulting 75th curve is closer to Trend 2, where the peak was found at 16.2%, the inflection point was found at 34.7%, and the associated value of the effusion rate at the inflection point was 71.0% of the peak (Figure 6).

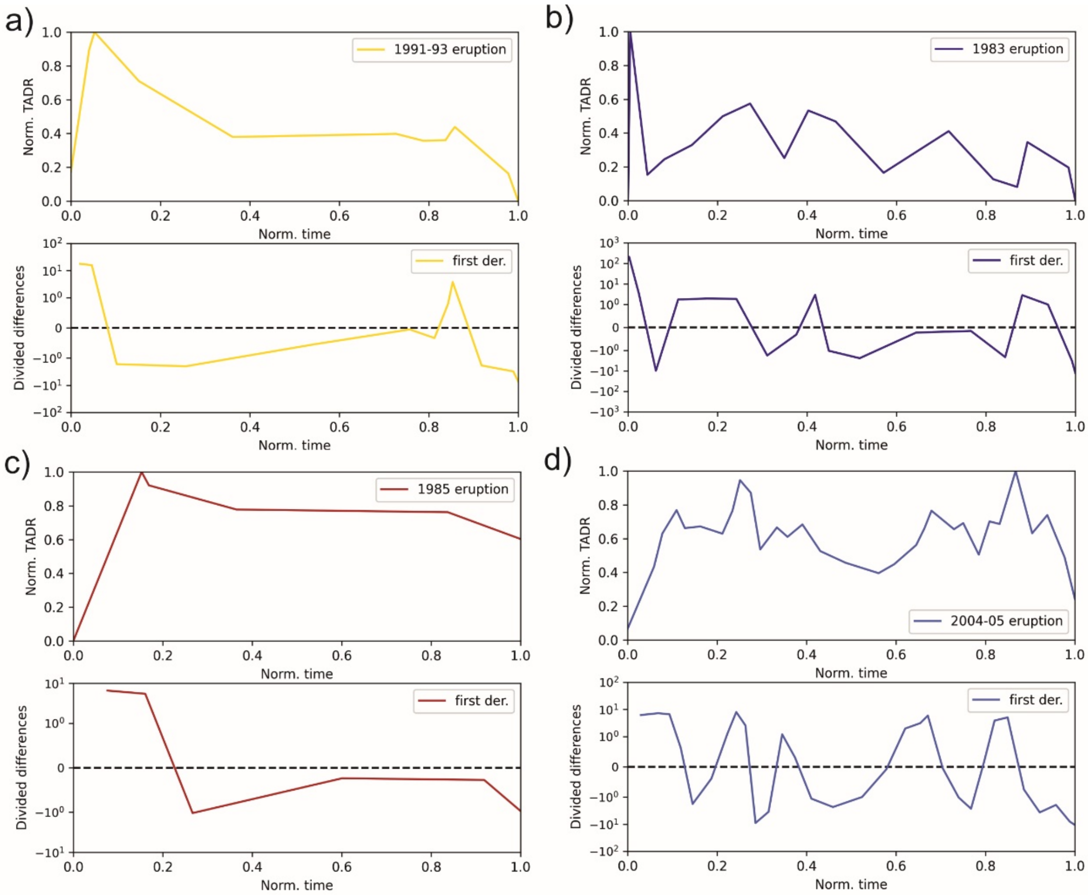

Figure 5. Examples of the first derivative calculations for the Trend 1 (**a**,**b**) and Trend 2 (**c**,**d**) TADR curves, where the inflection point is easily identified (**a**,**c**), while it is more difficult to identify the inflection point in more oscillating trends (**b**,**d**).

In order to use the "characteristic" curves in a model such as GPUFLOW, they must be de-normalized. If the given constraints are the total duration T (in seconds) of the eruption and the total volume of lava V (in m^3), then the de-normalized peak (t_{peak}) and inflection time (t_{infl}) can be found simply as $t_{peak} = t_{peak\_norm}{}^*T$ and $t_{infl} = t_{infl\_norm}{}^*T$. The peak of flux rate F_p (m^{3}s^{-1}) can be calculated as

$$F_p = \left(\frac{1}{c}\right)\left(\frac{V}{T}\right) \tag{1}$$

where c is the normalized volume, computed as

$$c = \frac{t_{peak\_norm}}{2} + \frac{\left(1 + TADR_{infl\_norm}\right)\left(t_{infl\_norm} - t_{peak\_norm}\right)}{2} + \frac{TADR_{infl\_norm}\left(1 - t_{infl\_norm}\right)}{2} \tag{2}$$

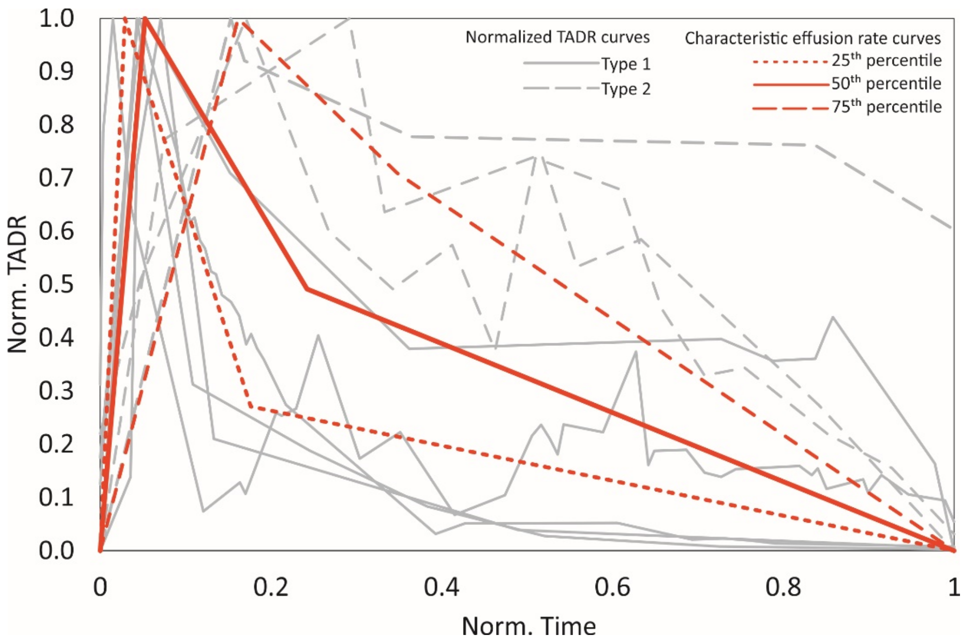

Figure 6. Diagram showing the "characteristic" effusion rate curves defined by the calculation of the 25th percentiles (dotted red line), 50th percentiles (solid red line) and 75th percentiles (dashed red line) of incidence of the effusion rate peaks and the inflection points from the normalized TADRs (solid grey line: Trend 1; dashed grey line: Trend 2).

Specifically, we have $c \simeq 0.22$ for the 25th curves, $c \simeq 0.36$ for the 50th curves, and $c \simeq 0.47$ for the 75th curves. The value of the effusion rate at the inflection point can then be computed as $F_{infl} = \mathrm{TADR}_{infl\_norm} {}^{*} F_p$ for each characteristic curve, while the effusion rate values at any given time during the running of the simulation are calculated by the linear interpolation of the fixed points. For this work, we calibrated all of the characteristic curves using the total durations and total volumes associated with the eruptive classes used for the assessment of the lava flows at Mt. Etna (Table 2), as defined by analyzing the distribution of the flow duration and volumes of more than fifty effusive eruptions which occurred during the last 400 years [10]. Both short- and long-lasting eruptions were considered in the definition of the eruptive classes, setting thresholds of the total durations at 30 and 90 days, while the thresholds of the total volumes of lava which erupted were fixed at 30, 100 and 200 $\times$ 10^6 m^3 [10]. The combination of the durations and volumes leads us to obtain six effusion rate curves for each characteristic curve (18 in total), where higher effusion rate peaks were calculated for the 25th characteristic curves compared to the corresponding 50th and 75th for each eruptive class. In this regard, the maximum value, up to 351 $m^3 s^{-1}$, is associated with class 5 (i.e., 200 $\times$ 10^6 m^3 of lava erupting in 30 days), derived from the 25th percentile curves, while the 50th and 75th percentiles curves show, respectively, values of 216 $m^3 s^{-1}$ and 164 $m^3 s^{-1}$ for the same eruptive class.

Table 2. Thresholds of the total durations and the lava volumes defined for each eruptive class associated with the flank eruptions (adapted from [10]).

Eruptive Classes	Total Time (Days)	Volume (m^3)
Class 1	30	30×10^6
Class 2	90	30×10^6
Class 3	30	100×10^6
Class 4	90	100×10^6
Class 5	30	200×10^6
Class 6	90	200×10^6

3.3. GPUFLOW Simulations

A total of 54 lava flow simulations generated by the six eruptive classes (Table 2) with the effusion rate curves derived from the three characteristic curves (Figure 6) were performed on three planes with variable inclinations (10°, 20°, 30°) by using the GPUFLOW model. All of the simulated lava flows are tongue-shaped, and are generally characterized by narrow channels in correspondence with the eruptive vent, becoming wider toward the front (Figure 7). This effect is more marked on the simulated lava derived from the 50th and 75th characteristic curves, which also show a greater thickness at the lava flow front on the plane at 10°. Few simulations performed at the same inclinations show small lateral flows close to the vent area that are symmetric with respect to the main flow direction. This effect is particularly evident in long-lasting simulations (90 days). The increase in the inclination of the planes produces a progressive increase of the lava flow thickness toward the vent area with narrower and thinner lava fronts. However, for hazard purposes, the most important features are the area and the run-out distance of the lava flows. In this regard, short-lasting simulations (30 days) originating from 25th percentiles show a positive correlation between the final lengths and the inclination of planes, whereas lava flows generated by using 75th curves are generally characterized by a negative correlation. Concerning lava flows derived from the 50th characteristic curve, the maximum lengths of lava flows are observed mostly for simulations performed on a plane inclination of 20° (Figure 8). In general, the length variations induced by plane inclinations are very limited.

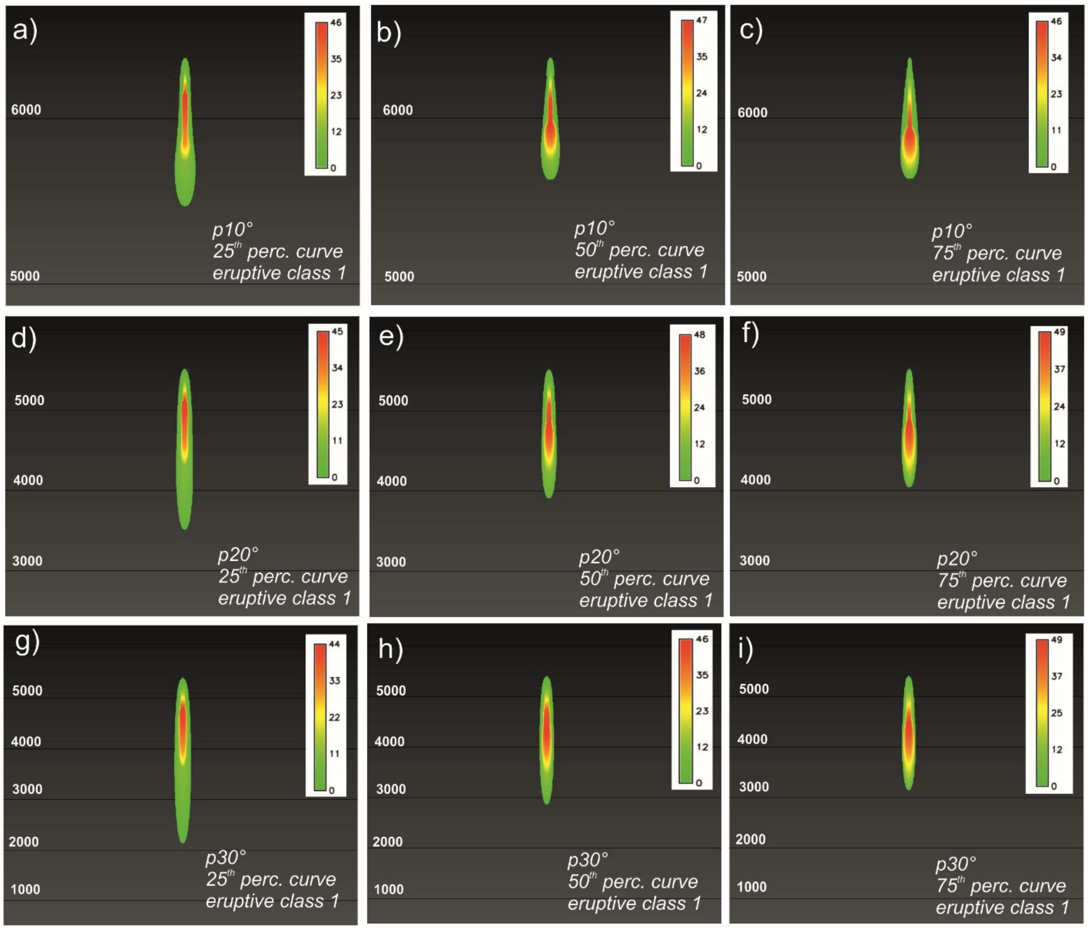

Figure 7. Results of the simulations showing the lava emplacement on inclined planes with slopes of 10° (**a**–**c**), 20° (**d**–**f**) and 30° (**g**–**i**), originating from 25th, 50th and 75th percentiles curves associated to the eruptive class 1 (i.e., 30×10^6 m^3 of lava erupted in 30 days). The thin lines represent the level curves associated with the inclined planes. The color bars indicate the thickness in meters of the simulated lava flows.

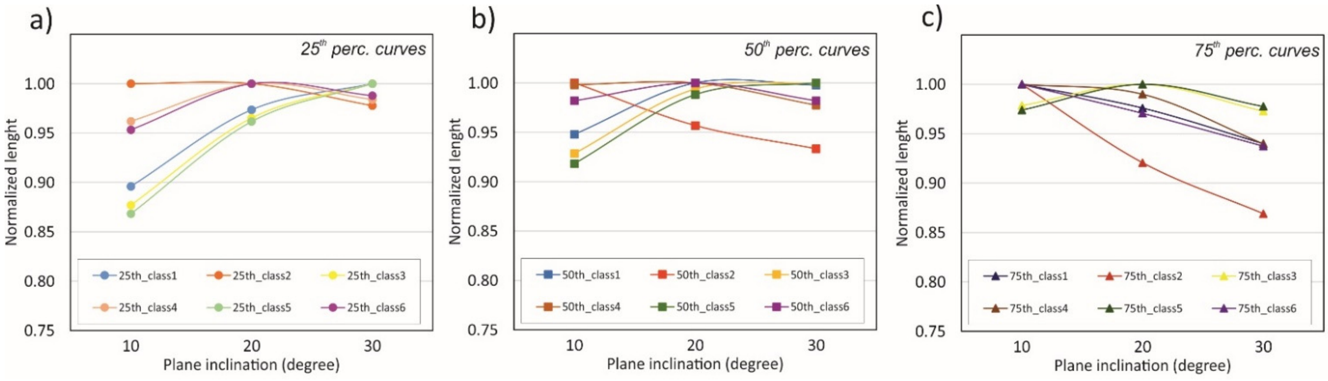

Figure 8. Diagrams showing the effects of the inclination of the planes on the lengths of the lava flows originating from the 25th (**a**), 50th (**b**) and 75th (**c**) percentile curves. The lengths were normalized with respect to the highest value estimated for each characteristic curve and the associated eruptive class.

The highest run-out distances were reached by the simulations using the 25th curves, which show a greater length than the simulated lava associated with the 50th and the 75th curves for the corresponding eruptive classes by factors of 1.20–1.29 and 1.22–1.45, respectively (Figure 9). The highest difference is observed between simulations derived from the 25th and 75th percentiles, which correspond to the eruptive class 1 on the 30° inclined plane (Figures 7 and 9). Conversely, the run-out distances obtained from 50th curves are longer than factors of 1.01–1.13 with respect to the 75th simulated lavas, suggesting that they reached similar lengths from the vent (Figure 8). The inclination of the planes induced a slightly greater difference in the length ratios, which was particularly evident between the simulations derived from 25th and 75th characteristic curves due to decoupled effects on the final lengths of lava flows at increasing plane inclinations.

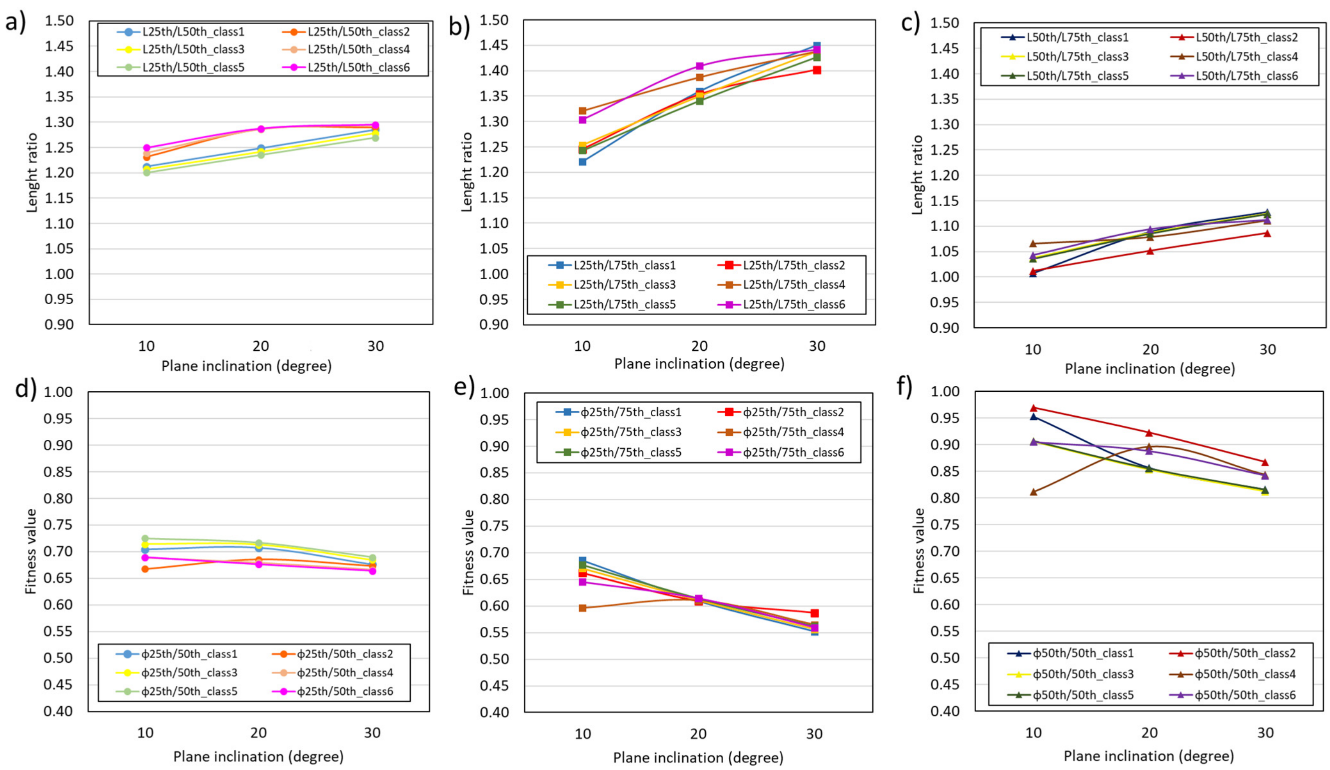

Figure 9. Diagrams showing the length ratios L (**a**–**c**) and fitness values ϕ (**d**–**f**) between simulated lava derived from the characteristic curves on all of the inclined planes (10°, 20°, 30°). Calculations were performed between the 25th and 50th curves (circles), the 25th and 75th curves (square), and the 50th and 75th curves (triangles) for each eruptive class.

The difference in the emplacements between the simulated lava flows was evaluated using the fitness value ϕ, which is a scalar value computed as the ratio between the intersection and the union of the areas covered by the simulated flows (given two lava flow areas A and B, the fitness value is calculated as $\phi = (A \cap B)/(A \cup B)$ [15]). Our tests revealed variations of 27–34% (ϕ = 0.66–0.73) between lava flows derived from the 25th and the 50th curves, while slightly greater variations of 32–44% (ϕ = 0.56–0.68; Figure 9) characterize the fitness value calculated between the 25th and the 75th simulations. On the contrary, the lava emplacements from the 50th and the 75th curves show variations of 3 –19%, providing very similar results (ϕ = 0.81–0.97; Figure 9).

An additional set of 18 simulations (six eruptive classes on the three inclined planes) were performed using the bell-shaped effusion rate curves adopted in [10], maintaining the same physical parameters for the lava and simulations. The simulated lava flows were then used as reference cases, and were compared with those obtained from the characteristic curves for each corresponding eruptive class and inclined plane. In these cases, the simulated lava generated from the 25th percentile characteristic curves also showed higher run-out distances than the simulations performed by using bell-shaped curves, with factors of 1.10–1.20 at 10° inclination, and a small increase of the length ratio was observed at higher inclinations of planes up to 1.36 (Figure 10). Conversely, 50th and 75th are generally slightly shorter, by a factor up to 0.88, and some simulated flows derived from the 50th percentile characteristic were slightly longer than the corresponding lava flow derived from the bell-shaped curve on the plane with inclination of 20°–30° (with a factor of up to 1.06). Concerning the fitness value for the areas, variations of up to 39% (ϕ = 0.61) were observed between the lava flows derived from the 25th percentile and the bell-shaped curves (Figure 10). Such differences are smaller for the 50th and the 75th percentiles (ϕ = 0.75–0.91), indicating that the simulated flows cover more similar areas.

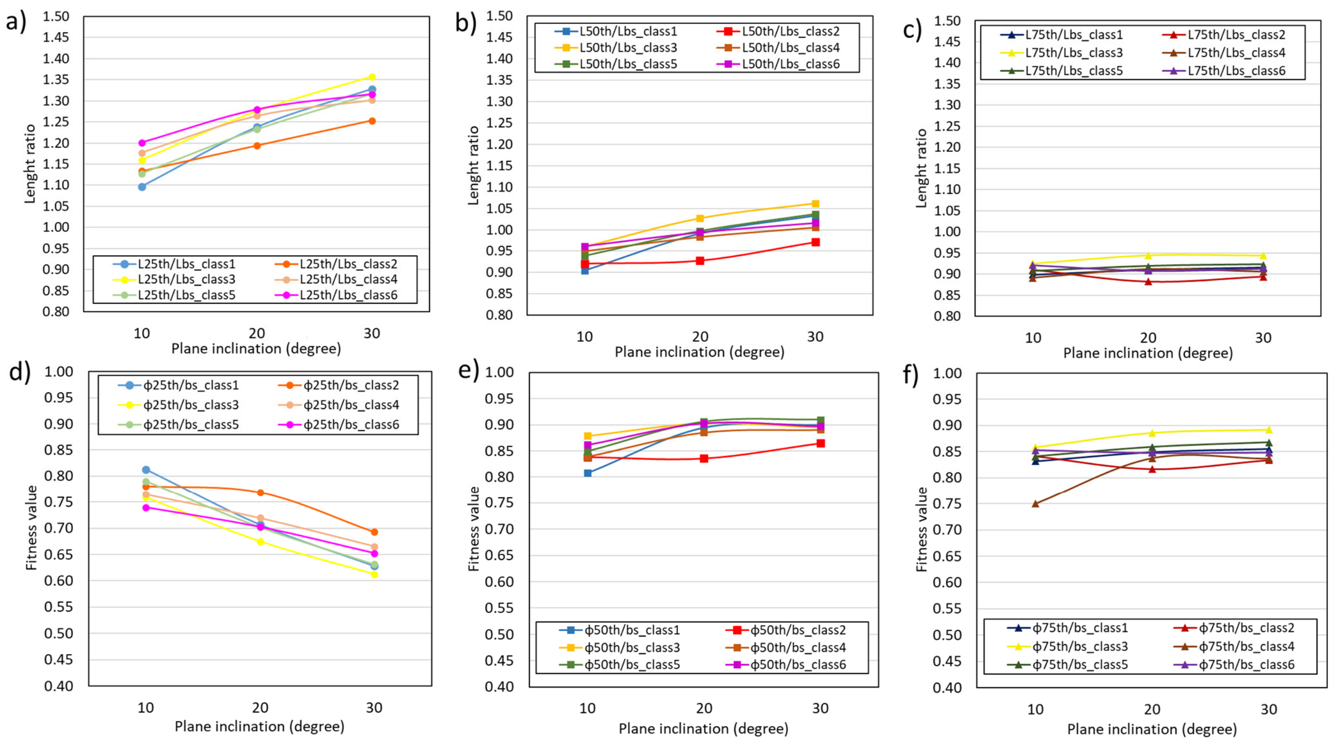

Figure 10. Diagrams showing the length ratios L (**a**–**c**) and fitness values ϕ (**d**–**f**) between the simulated lava derived from the characteristic curves and bell-shaped (bs) curves on all of the inclined planes (10°, 20°, 30°). Calculations were performed to compare the 25th curves (circles), 50th (square), and 75th curves (triangles) with the bell-shaped curves for each eruptive class.

4. Discussion

The analysis of the TADR time series allowed us to obtain insights into the dynamics of the lava flow emplacement during flank eruptions at Mt. Etna. The incidence of the effusion rate peaks at the beginning of the eruptions reflects that more than 50% of the lava volume erupts in the first 10–40% of the total duration, followed by an overall decrease in the discharge rates. This trend is consistent with the release of the energy stored in the reservoir through elastic deformation induced by magmatic overpressurization [13]. The modification of the conduit shape and the dynamics of the magma supply from the depths, which are additional factors that control the rate at which lava is discharged [13], may be responsible for the differences in the total duration and shape of the analyzed TADR time series, as well as between the Trend 1 and Trend 2 curves. Indeed, the unusually high discharge rate estimated for the 1981 eruption (up to 641 m^3s^{-1}) was explained as a complex interaction between a shallow magma reservoir with a dike intrusion from the deeper part of the plumbing system [17]. Fluctuations in the convoluted curves can be attributed to pulses of lava supply from the reservoir, leading to deviations of the effusion rate from the theoretical trend. In the case of the 2001 eruption, different eruptive vents were developed both on the summit-subterminal and flank areas, which were linked to distinct magma pathways [37]. Thus, the potential dispersal of the energy linked to the separated pathways through which the magma reached the surface may have induced the observed differences in the TADR curve shape from Trend 1 for the 2001 eruption. On the other hand, the atypical behavior of the 1985 and 1986–87 eruptions, characterized by a rather low averaged effusion rate and a high average/peak ratio, may highlight an absence of an energetic phase during the eruption with high lava discharge rates. However, it is note that measurements of thermal infrared data from the AVHRR sensor during the first 8–15 days from the beginning of the eruptive activity are lacking for the 1985 and 1986–87 eruptions. Therefore, we cannot exclude the possibility that higher TADRs values could have characterized the lava effusion for these two events, showing that the expected effusion rate curves could be more similar to Trend 1. Finally, the opposite trend which was observed for the 2004–05 eruption can be attributed to the different dynamics triggering the eruption, which were mainly controlled by the response of the eastern flanks induced by the regional geodynamic stress, with a very poor contribution from the magmatic overpressure [31,38]. Such inferences lead us to give more emphasis to the simulations performed using effusion rate curves converted from the 25th characteristic curve, as they are is closer to the pattern shown by Trend 1, which includes the most hazardous events of the last century at Mt. Etna (i.e., the 1928, 1981 and 1991–93 eruptions). We observed that the earlier the achievement of the peak, the higher the effusion rate at the same expected volume of lava erupted and total time of the eruption, thereby leading to higher values of the theoretical effusion rate peak in the 25th curves compared to the 50th and 75th curves at corresponding eruptive classes. Similarly, the bell-shaped curves used for the definition of the lava flow hazard map [10] are characterized by a lower maximum effusion rate than the corresponding 25th percentile characteristic curves. This feature played a key role in the final results achieved by simulating the lava emplacement through the GPUFLOW model. In fact, the general behavior of lava emplacement reproduced by using the 50th and 75th characteristic curves is more consistent with that of the reference cases linked to the bell-shaped curves, whereas higher run-out distances were obtained for simulations performed using the 25th percentiles.

Though steeper slopes cause a moderate shortening of the lava lengths when using the 50th and 75th characteristic curves, this was not observed for lava flows produced with the 25th characteristic curve in short-lasting simulations (30 days). Such a feature is due to the relatively faster cooling of the thinner lava front induced by a higher contribution of the gravity-driven flow at greater inclinations for simulated lava associated with the 50th and 75th characteristic curves. On the contrary, the higher effusion rates estimated for the corresponding 25th curves reduce the cooling effects, allowing lava flows to reach greater distances during the early phases of the eruption, thereby leading to the low estimated fitness values between the lava emplacements originating from the 25th and 50th/75th curves. Similarly, the presence of small lateral flows close to the vent in some long-lasting simulations (90 days) on the inclined plane with a slope of 10° can be attributed to the relatively lower effusion rates compared to the corresponding short-lasting simulations with the same expected volume of lava erupted; this, combined with a lower slope, allows cooling effects to influence the emplacement more strongly during the waning phase. Even though the presence of lateral flows testifies to the influence of cooling during the emplacement of lava flows generated using the 25th percentile curve for the corresponding erupted class 2 (i.e., 30×10^6 m^3 of lava erupted in 90 days), the simulated lava covered a greater distance than lava flows produced by using the bell-shaped curve from [10] for the same eruptive class (Figure 11a). Conversely, the lava flows associated with the 50th and 75th percentiles reached shorter distances from the vent compared to the reference case (Figure 11b,c).

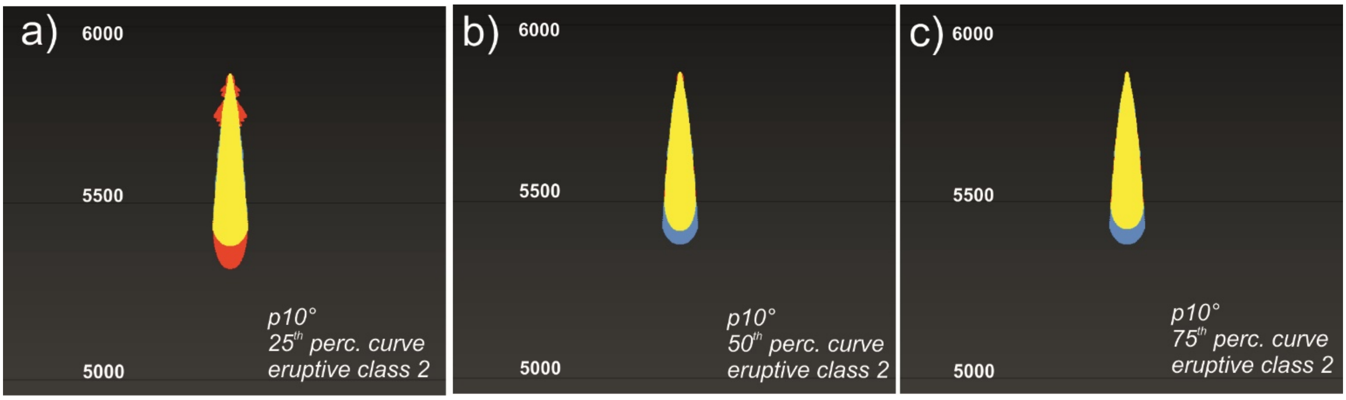

Figure 11. Graphical representation of the fitness value, overlaying test simulations obtained by using the 25th (**a**), 50th (**b**) and 75th (**c**) percentile curves associated to the eruptive class 2, with emplacements produced by using bell-shaped curve for the same eruptive class used as a reference. Yellow represents the common inundated areas, red represents the overestimated areas (inundation from tests but not from the reference) and blue represents the underestimated areas (inundation from the reference but not from the tests). The lava flow originating from the 25th percentile curve show small lateral overflows due to cooling effects during the waning phase.

Our tests confirm that the greater lengths of the lava flows from the vent are positively correlated with higher effusion rates. This implies that the impact of lava emplacement is mainly controlled by the temporal evolution of the lava effusion rates at given boundary conditions (e.g., the same total duration and total volume of erupted lava, emission temperature, and water concentration). Such results have a significant repercussion on the management of the hazard linked to the Etnean flank eruptions, as the early phases are crucial for the determination of the extent of a lava flow.

The main limitation of our analysis is that the effusion rate curves are only available for a small number of Etnean flank eruptions. Thus, a better characterization of such hazardous events can be derived by collecting more TADR time series data for historical eruptions, e.g., through a topographic approach. Our future work will also include the analysis and characterization of the eruptive episodes producing lava flows that occurred at the summit craters, which can threaten the touristic facilities located on the volcano flanks, i.e., damage to which could negatively affect the local economy.

5. Conclusions

An analysis of the lava discharge rate time series was performed for recent flank eruptions at Mt. Etna in order to define a generalized trend of lava effusion rates in time. In total, 90% of the analyzed case studies showed that the peak of the effusion rate occurs in the first 30% of the total duration of the eruption, which is then characterized by a general decrease of the volume flux until the end of the eruption. In order to represent the main variability in the observed real curves, three generalized curves were built with variable positions of the effusion rate peaks. Lava flow modeling was then performed on planes with various inclinations using theoretical effusion rate curves derived from these characteristic curves for a fixed total volume of lava erupted and the total duration in order to evaluate the effects of time variations in the effusion rate coupled with the inclination of the substrate on the emplacement of lava flows. The results were compared with simulations based on the bell-shaped effusion rate curves used to develop one of the most recent lava flow hazard maps at Mt. Etna [10]. From the analysis, we observed that bell-shaped curves reproduce well the general behavior of lava effusion rates linked to the flank eruptions of Mt. Etna, as differences in the lengths of the simulated lava flows from those produced by using the characteristic curves are of the order of 5–10%. However, a category of eruptive events characterized by a relatively early occurrence of the effusion rate peak with exceptionally high values leads to greater lengths of simulated lava flows than the reference cases, with variations of up to 20%. At a higher inclination of the planes, an increase of length of up to 35–40% is observed. This category is well represented by very short-lasting events, such as the 1928, 1981 and 2018 eruptions (4–15 days), though their probability of occurrence is low. This contributes to increasing the volcanic hazard linked to lava flows for flank eruptions at Mt. Etna, due to the relatively high velocities of flowing lava erupting in a short time, and the potentially greater distances reached compared to those predicted from the lava flow hazard map. Adding this category of effusion rate curve will allow a better evaluation of the impact of lava flow inundation for real-time applications, as well as an update of the lava flow hazard map at Mt. Etna, where the probability of lava inundation is obtained by combining the numerical simulations with the spatiotemporal probability of future vent opening and the occurrence probability of the expected eruptive classes of eruptions.

The results obtained through our effusion rate analysis allowed us to obtain insights into the dynamics of flank eruptions at Mt. Etna, and for lava flow hazard assessment. We found that more than 50% of the lava volume is emitted at the very beginning of an eruption, consistent with the overpressurization of the magmatic reservoir, which may lead to the rapid achievement of the effusion rate peak at the initial phase of eruptions. The nearly exponential decrease is determined by the release of elastic strain energy stored in the reservoir. Moreover, our analysis is fundamental for the evaluation of both the short- and long-term hazard due to lava flows, playing a role in risk mitigation in densely populated areas in close proximity to active volcanoes. Although it was conducted on Mt. Etna, the approach is designed to be applicable to other volcanic areas where an extensive dataset of effusion rate temporal series is available.

Author Contributions: Conceptualization, F.Z. and G.G.; Data curation, G.B., G.G. and A.C.; Formal analysis, F.Z., Funding acquisition, A.C.; Methodology, G.B. and G.G.; Software, F.Z. and G.B.; Validation, F.Z., G.B. and A.C.; Writing—original draft, F.Z., G.B., G.G. and A.C. All authors have read and agreed to the published version of the manuscript.

Funding: This work was supported by the INGV project Pianeta Dinamico (CUP D53J19000170001) funded by MIUR ("Fondo finalizzato al rilancio degli investimenti delle amministrazioni centrali dello Stato e allo sviluppo del Paese," legge 145/2018), Tema 8–PANACEA 2021.

Data Availability Statement: Not applicable.

Acknowledgments: We thank the editor David Gomez-Ortiz and the three anonymous reviewers for their constructive and supportive comments, which helped improve this manuscript.

Conflicts of Interest: The authors declare no conflict of interest.

References

1. Crisci, G.; Gregorio, D.; Pindaro, O.; Ranieri, G. Lava flow simulation by a discrete cellular model: First implementation. *Int. J. Simul. Model.* **1986**, *6*, 137–140. [CrossRef]
2. Miyamoto, H.; Sasaki, S. Simulating lava flows by an improved cellular automata method. *Comput. Geosci.* **1997**, *23*, 283–292. [CrossRef]
3. Avolio, M.V.; Crisci, G.M.; Gregorio, S.D.; Rongo, R.; Spataro, W.; Trunfio, G.A. SCIARA g2: An improved cellular automata model for lava flows and applications to the 2002 Etnean crisis. *Comput. Geosci.* **2006**, *32*, 876–889. [CrossRef]
4. Cappello, A.; Hérault, A.; Bilotta, G.; Ganci, G.; Del Negro, C. MAGFLOW: A physics-based model for the dynamics of lava-flow emplacement. *Geol. Soc. Lond. Spec. Publ.* **2016**, *426*, 357–373. [CrossRef]
5. Vicari, A.; Herault, A.; Del Negro, C.; Coltelli, M.; Marsella, M.; Proietti, C. Simulations of the 2001 lava flow at Etna volcano by the Magflow cellular automata model. *Environ. Model. Softw.* **2007**, *22*, 1465–1471. [CrossRef]
6. Vicari, A.; Ganci, G.; Behncke, B.; Cappello, A.; Neri, M.; Del Negro, C. Near-real-time forecasting of lava flow hazards during the 12–13 January 2011 Etna eruption. *Geophys. Res. Lett.* **2011**, *38*, 13. [CrossRef]
7. D'Ambrosio, D.; Filippone, G.; Rongo, R.; Spataro, W.; Trunfio, G.A. Cellular automata and GPGPU: An application to lava flow modeling. *Int. J. Grid High Perform. Comput.* **2012**, *4*, 18. [CrossRef]
8. Cappello, A.; Ganci, G.; Bilotta, G.; Herault, A.; Zago, V.; Del Negro, C. Satellite-driven modeling approach for monitoring lava flow hazards during the 2017 Etna eruption. *Ann. Geophys.* **2019**, *62*, 2. [CrossRef]
9. Favalli, M.; Mazzarini, F.; Pareschi, M.T.; Boschi, E. Topographic control on lava flow paths at Mount Etna, Italy: Implications for hazard assessment. *J. Geophys. Res. Earth Surf.* **2009**, *114*, F01019. [CrossRef]
10. Del Negro, C.; Cappello, A.; Neri, M.; Bilotta, G.; Hérault, A.; Ganci, G. Lava flow hazards at Mount Etna: Constraints imposed by eruptive history and numerical simulations. *Sci. Rep.* **2013**, *3*, 3493. [CrossRef]
11. Walker, G.P.L. Lengths of lava flows. *Phil. Trans. R. Soc. Lond.* **1973**, *274*, 107–118.
12. Harris, A.J.L.; Rowland, S.K. Effusion rate controls on lava flow length and the role of heat loss: A review. *Geol. Soc. Lond. Spec. Publ.* **2009**, *2*, 33–51.
13. Wadge, G. The variation of magma discharge during basaltic eruptions. *J. Volcanol. Geotherm. Res.* **1981**, *11*, 139–168. [CrossRef]
14. Harris, A.; Steffke, A.; Calvari, S.; Spampinato, L. Thirty years of satellite-derived lava discharge rates at Etna: Implications for steady volumetric output. *J. Geophys. Res.* **2011**, *116*, B08204. [CrossRef]
15. Bilotta, G.; Cappello, A.; Hérault, A.; Vicari, A.; Russo, G.; Del Negro, C. Sensitivity analysis of the MAGFLOW cellular automaton model for lava flow simulation. *Environ. Model. Softw.* **2012**, *35*, 122–131. [CrossRef]
16. Harris, A.J.L.; Dehn, J.; Calvari, S. Lava effusion rate definition and measurement: A review. *Bull. Volcanol.* **2007**, *70*, 1. [CrossRef]
17. Coltelli, M.; Marsella, M.; Proietti, C.; Scifoni, S. The case of the 1981 eruption of Mount Etna: An example of very fast moving lava flows. *Geochem. Geophys. Geosyst.* **2012**, *13*, Q01004. [CrossRef]
18. Branca, S.; De Beni, E.; Proietti, C. The large and destructive 1669 AD Etna eruption: Reconstruction of the lava flow field evolution and effusion rate trend. *Bull. Volcanol.* **2013**, *75*, 2–16. [CrossRef]
19. Branca, S.; De Beni, E.; Chester, D.; Duncan, A.; Lotteri, A. The 1928 eruption of Mount Etna (Italy): Reconstructing lava flow evolution and the destruction and recovery of the town of Mascali. *J. Volcanol. Geotherm. Res.* **2017**, *335*, 54–70. [CrossRef]
20. Harris, A.J.L.; Blake, S.; Rothery, D.A.; Stevens, N.F. A chronology of the 1991 to 1993 Mount Etna eruption using advanced very high resolution radiometer data: Implications for real-time thermal volcano monitoring. *J. Geophys. Res.* **1997**, *102*, 7985–8003. [CrossRef]
21. Wright, R.; Blake, S.; Harris, A.J.; Rothery, D.A. A simple explanation for the space-based calculation of lava eruption rates. *Earth Planet. Sci. Lett.* **2001**, *192*, 223–233. [CrossRef]
22. Ganci, G.; Bilotta, G.; Cappello, A.; Hérault, A.; Del Negro, C. HOTSAT: A multiplatform system for the satellite thermal monitoring of volcanic activity. *Geol. Soc. Lond. Spec. Publ.* **2016**, *426*, 207–221. [CrossRef]
23. Ganci, G.; Cappello, A.; Bilotta, G.; Hérault, A.; Zago, V.; Del Negro, C. Mapping volcanic deposits of the 2011–2015 Etna eruptive events using satellite remote sensing. *Front. Earth Sci.* **2018**, *6*, 83. [CrossRef]
24. Kaneko, T.; Yasuda, A.; Fujii, T. Simple empirical method for estimating lava-effusion rate using nighttime Himawari-8 1.6-µm infrared images. *Earth Planets Space* **2021**, *73*, 37. [CrossRef]
25. Cappello, A.; Ganci, G.; Calvari, S.; Pérez, N.M.; Hernández, P.A.; Silva, S.V.; Cabral, J.; Del Negro, C. Lava flow-hazard modeling during the 2014–2015 Fogo eruption, Cape Verde. *J. Geophys. Res. Solid Earth* **2016**, *121*, 2290–2303. [CrossRef]
26. Harris, A.J.L.; Villeneuve, N.; Di Muro, A.; Ferrazzini, V.; Peltier, A.; Coppola, D.; Favalli, M.; Bachèlery, P.; Froger, J.L.; Gu-rioli, L.; et al. Effusive crises at Piton de la Fournaise 2014–2015: A review of a multi-national response model. *J. Appl. Volcanol.* **2017**, *6*, 11. [CrossRef]
27. Branca, S.; Del Carlo, P. Types of eruptions of Etna volcano AD 1670–2003: Implications for short-term eruptive behaviour. *Bull. Volcanol.* **2005**, *67*, 732–742. [CrossRef]
28. Cappello, A.; Bilotta, G.; Neri, M.; Del Negro, C. Probabilistic modeling of future volcanic eruptions at Mount Etna. *J. Geophys. Res. Earth Surf.* **2013**, *118*, 1925–1935. [CrossRef]
29. Ganci, G.; Vicari, A.; Fortuna, L.; Del Negro, C. The HOTSAT volcano monitoring system based on combined use of SEVIRI and MODIS multispectral data. *Ann. Geophys.* **2011**, *54*, 544–550. [CrossRef]

30. Rogic, N.; Bilotta, G.; Ganci, G.; Thompson, J.O.; Cappello, A.; Rymer, H.; Ramsey, M.S.; Ferrucci, F. The impact of dynamic emissivity-temperature trends on spaceborne data of the 2001 Mount Etna eruption. *Remote Sens.* 2022; *submitted*.
31. Del Negro, C.; Cappello, A.; Ganci, G. Quantifying lava flow hazards in response to effusive eruption. *GSA Bull.* **2016**, *128*, 752–763. [CrossRef]
32. Ganci, G.; Vicari, A.; Cappello, A.; Del Negro, C. An emergent strategy for volcano hazard assessment: From thermal satellite monitoring to lava flow modeling. *Remote Sens. Environ.* **2012**, *119*, 197–207. [CrossRef]
33. Calvari, S.; Bilotta, G.; Bonaccorso, A.; Caltabiano, T.; Cappello, A.; Corradino, C.; Del Negro, C.; Ganci, G.; Neri, M.; Pecora, E.; et al. The VEI 2 Christmas 2018 Etna eruption: A small but intense eruptive event or the starting phase of a larger one? *Remote Sens.* **2020**, *12*, 905. [CrossRef]
34. PeakFit—The Automatic Choice For Spectroscopy, Chromatography and Electrophoresis, Trial Version. Available online: http://www.sigmaplot.co.uk/products/peakfit/peakfit.php (accessed on 24 September 2021).
35. Bilotta, G.; Ganci, G.; Cappello, A. Modelling of geophysical flows through GPUFLOW. *Appl. Sci.* 2022; *manuscript in preparation*.
36. Del Negro, C.; Fortuna, L.; Herault, A.; Vicari, A. Simulations of the 2004 lava flow at Etna volcano using the magflow cellular automata model. *Bull. Volcanol.* **2008**, *70*, 805–812. [CrossRef]
37. Viccaro, M.; Ferlito, C.; Cortesogno, L.; Cristofolini, R.; Gaggero, L. Magma mixing during the 2001 event at Mt. Etna (Italy): Effects on the eruptive dynamics. *J. Volcanol. Geotherm. Res.* **2006**, *149*, 139–159. [CrossRef]
38. Burton, M.; Neri, M.; Andronico, D.; Branca, S.; Caltabiano, T.; Calvari, S.; Corsaro, R.A.; Del Carlo, P.; Lanzafame, G.; Lodato, L.; et al. Etna 2004–2005: An archetype for geodynamically-controlled effusive eruptions. *Geophys. Res. Lett.* **2005**, *32*, 9. [CrossRef]